

# **Potential of enhanced weathering of calcite in packed bubble columns with seawater for carbon dioxide removal**

Lei Xing<sup>1</sup>, Huw Pullin<sup>2</sup>, Liam Bullock<sup>1</sup>, Phil Renforth<sup>3\*</sup>, Richard C. Darton<sup>1</sup>, Aidong Yang<sup>1\*</sup>

1. Department of Engineering Science, University of Oxford, Oxford, OX1 3PJ, United Kingdom
2. School of Earth and Ocean Sciences, Cardiff University, Cardiff CF10 3AT, United Kingdom
3. School of Engineering and Physical Sciences, Heriot-Watt University, Edinburgh EH14 4AS, United Kingdom

\* Corresponding authors:

[p.renforth@hw.ac.uk](mailto:p.renforth@hw.ac.uk) (P. R.)

[aidong.yang@eng.ox.ac.uk](mailto:aidong.yang@eng.ox.ac.uk) (A.Y.)

## **Abstract**

Enhanced weathering of minerals is one option being considered for removing CO<sub>2</sub> from the atmosphere to help combat climate change. In this work, we consider the weathering of calcite with seawater in a reactor using air enriched with CO<sub>2</sub>. A mathematical model of the packed bubble column reactor was constructed with the key mass transfer and chemical reaction components validated with experimental data. The modelling results for a continuous process reveal the performance in terms of the specific energy consumption and the CO<sub>2</sub> capture rate, which are affected by parameters including particle size, superficial velocities of gas and liquid, reactor bed height and feed CO<sub>2</sub> concentration. The major energy requirements are for pumping liquid and compressing gas, and for CO<sub>2</sub> enrichment; energy needed for supplying solid particles (mining operations, transport and comminution) was found to be comparatively minor. A trade-off was possible between ground area requirement (determined by CO<sub>2</sub> capture rate) and energy requirement. To capture 1 tonne of CO<sub>2</sub> at the reactor, optimal designs were predicted to consume 2.1-2.3 GJ of electricity and occupy 1.8-5.2 m<sup>2</sup> year of space, depending on the feed CO<sub>2</sub> concentration. These would increase to 5.7-8.2 GJ and 7.1-13.1 m<sup>2</sup> year per tonne of CO<sub>2</sub> captured, after allowing for degassing of the weathering product in the ocean. This increased energy intensity is still within the range of the CO<sub>2</sub> removal options previously reported, while the space requirement quantification provides essential information for future feasibility assessment of this scheme.

**Keywords:** enhanced weathering, carbon dioxide removal, packed bubble column, mathematical modelling, energy consumption, space requirement

## 1. Introduction

To combat climate change, many important measures are being adopted to reduce greenhouse gas emissions, including replacing fossil fuels with renewable energy, reducing emissions through efficiency improvement and demand reduction, and capturing the gases at source. In addition, it is calculated that limiting global warming to the target of 1.5°C would require carbon dioxide removal from the atmosphere (CDR) of some 100 - 1000 GtCO<sub>2</sub> over the 21<sup>st</sup> century [1], which could be achieved through a wide range of methods [2-3].

As one of the CDR options, enhanced weathering (EW) of carbonate or silicate minerals [4] aims at accelerating the natural weathering process which is known to draw down a significant amount of CO<sub>2</sub> from the atmosphere through the reaction between the rock, CO<sub>2</sub> and water [5], but at a very slow pace. EW might be implemented by spreading crushed minerals in specific natural environments such as on the soil [6, 7] or in coastal areas [8]. Compared to such “natural” deployments, options in which mineral particles are weathered in engineered reactors [9-11], where conditions are more controlled, could lead to benefits such as higher CDR rates and fewer unpredictable interactions with the natural environment. However, these benefits might involve greater energy and water consumption [11] or other costs, which need to be quantified to assess the potential of such schemes.

In this work, packed bubble column (PBC) reactors are considered for weathering of calcite. A PBC reactor comprises a packed bed of mineral particles, with a continuous liquid phase filling most of the void space in the bed, and a gas flow travelling through the bed in the form of discrete bubbles. PBCs have been used for various purposes in the chemical industry and resemble the experimental device used in some early EW studies [9]. However, detailed investigations of PBCs for EW have been very limited to-date. To ameliorate the water consumption issue in a reactor-based scheme [11], the use of seawater is investigated here as a possibly feasible alternative to freshwater. Thermodynamically, a partial pressure of CO<sub>2</sub> ( $p\text{CO}_2$ ) higher than the atmospheric level is then required to achieve dissolution of calcite particles, because of the high level of saturation of calcite in seawater [12]. This means that the ambient air needs to be enriched in CO<sub>2</sub> before it can be fed to the weathering reactor.

The objective of this work is to assess PBC-based calcite weathering in seawater through the impact of the operational settings including particle size, gas and liquid flowrates and reactor height on CO<sub>2</sub> capture rate and energy consumption. The choice of CO<sub>2</sub> concentration of the gas feed has also been considered as an important factor: a higher concentration provides greater mass transfer driving force; however, it requires more energy for the enrichment step and potentially leads to more severe degassing of the weathering product when exposed to the ambient conditions, hence representing interesting trade-offs. A detailed mathematical model of the PBC reactor is constructed. The PBC model has been validated with lab-scale experiments, which are introduced first (Section 2.1) followed by the presentation of the reactor model (Section 2.2) and energy usage calculation (Section 2.3) and the results of model validation and simulation-based assessment (Section 3).

## **2. Methodology**

### **2.1 Experiments**

As show in Fig. 1, the weathering reaction occurred in a glass reactor vessel of volume 18 L and diameter 14.5 cm, consisting of three sections: the packed bed layer (a mixture of solid particles and seawater) at the bottom, the bubble column layer (seawater only) in the middle, and the headspace (gas only) at the top. 1.0 kg of limestone (predominantly calcite) particles, with two particle sizes of 0.5 and 5 mm, were weathered in seawater at 20°C, maintained by a glass jacket operating with a water flow. Seawater was collected from Dunraven Bay, South Wales, UK, and filtered to achieve the salinity of 35‰. During the experiments, a certain volume of the abovementioned seawater (either ~3.14 L or ~1.57 L) was added to maintain a high (~1:4.4) or low (~1:10) volume ratio of liquid to gas, respectively. Pressure in the headspace was maintained at 1 atm. The circulating reactant gas (CO<sub>2</sub>-N<sub>2</sub> mixture) was withdrawn from the headspace at two volumetric flow rates, 0.5 and 1.0 L min<sup>-1</sup> and re-introduced to the reactor through a sparger at the bottom of the packed bed. Two different initial gas compositions were used, with 5% and 50 % (v/v) CO<sub>2</sub>. Composition in the headspace was monitored continuously using a Gem Scientific G110 infrared CO<sub>2</sub> analyser (calibrated to ISO17025 ±1% accuracy), and 100 mL liquid was sampled periodically by an external peristaltic pump for alkalinity measurement. The same volume of the initial seawater was added

into the reactor following each sampling to maintain the total liquid volume. The weathering reaction was allowed to proceed for 120 mins and 8 liquid samples were withdrawn in total. The X-ray diffraction of the limestone in this work and further details of the experiments are provided in [Section S1](#) of Supporting Information (SI).

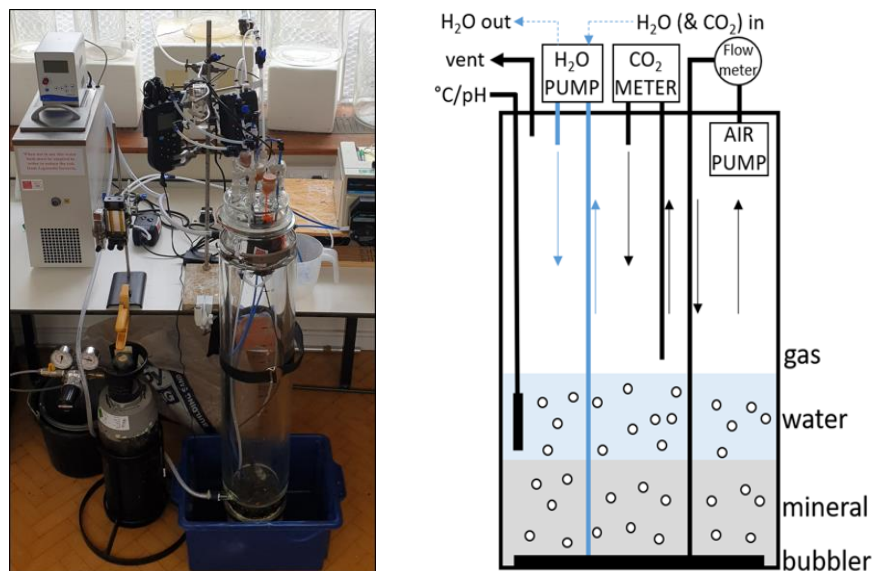


Fig. 1. Experimental setup (left) and schematic diagram (right)

## 2.2. Mathematical model development

### 2.2.1 The two PBC reactor models: material balances

A model was first developed for the PBC reactor used in the experimental work. The *experimental reactor* model describes the three PBC segments: a lower packed bed layer (*pbl*, mineral particles, water and bubble three-phase domain), an upper bubble column layer (*bcl*, water and bubble two-phase domain) and the top gas chamber (gas only). A gas flow circulates from the gas chamber to the bottom of the packed bed layer. This model, after validation using experimental data, was subsequently modified to form the *continuous reactor* model for a reactor with continuous, counter-current flow of liquid (seawater) and gas (CO<sub>2</sub>-enriched air). As shown in [Fig. 2](#), the gas flow leaving the top of the continuous reactor is not directly recirculated to the bottom of the reactor. Instead, it is enriched to a specified feed CO<sub>2</sub> concentration and then combined with the top-up CO<sub>2</sub>-enriched gas flow produced from ambient air to form the gas feed to

the reactor. Furthermore, the continuous reactor model includes only the packed bed layer because in this reactor absorption from the headspace is negligible (hence not modelled), and calculations suggested that having a bubble column layer on top of the packed bed layer would not be beneficial for CO<sub>2</sub> capture. However, the models for chemical reaction kinetics and gas-liquid mass transfer in the packed bed layer are identical between the two models. More details for modelling the experimental reactor could be found in [Section S2.1](#) of SI. Unless stated otherwise, the details presented below apply to both reactor models.

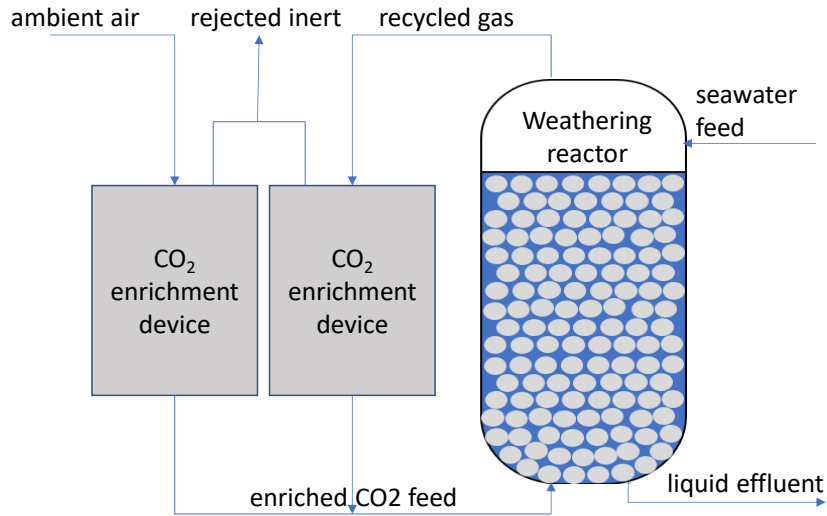


*Fig. 2. Sketch of continuous operation of the packed bubble column reactor*

Main assumptions of the models are as follows:

- Mineral particles are loaded into the reactor at the start of the operation without further replenishment.
- Isothermal operations are assumed, as the effect of reaction heat is negligible in the modelled reactors due to the huge amount of water required compared to the extent of the weathering reaction; the operating temperature was set to 20 °C.
- Spatial variation of concentrations occurs only along the height of the cylindrical packed bed; no radial gradients of concentration or velocity were considered.
- An average particle-shrinking rate was applied to all calcite particles, independent of the location inside the packed bed. The particles retain their shape (assumed spherical) during dissolution.

- Our earlier study [11] showed insignificant chemical acceleration of calcite weathering to carbon dioxide absorption due to the only weakly alkaline condition, which was therefore ignored in this work.
- A representative seawater composition with a salinity of ~35 was adopted (Section S2.2 of SI).

Key equations and principles of reactor modelling are presented here; further details (including additional model equations and all the parameter values adopted) can be found in Section S2 of SI. In the packed bed and bubble column layers (the latter relevant only to the experimental reactor), diffusive and dispersive mass transport of gaseous CO<sub>2</sub> is omitted because it is negligible in comparison with convective mass transport (Peclet number  $\gg 1$ ). An unsteady state mass balance for CO<sub>2(g)</sub> over the two layers yields the following equation:

$$\varepsilon_G \frac{\partial}{\partial t} c_{CO_2(g)} + \nabla \cdot (u_G c_{CO_2(g)}) = -r_{G-L} \quad (1)$$

where  $\varepsilon_G$  (-) is the gas holdup, defined as the volume fraction of either the packed bed layer or bubble column layer occupied by the gas phase,  $r_{G-L}$  (mol m<sup>-3</sup> s<sup>-1</sup>) is the source term, representing transfer of CO<sub>2</sub> from gas to liquid,  $u_G$  (m s<sup>-1</sup>) is the gas superficial velocity. In all the modelled cases, the change of volumetric flowrate of the gas stream along the reactor due to the absorption of CO<sub>2</sub> is negligible, but the impact of pressure drop must be considered as the pressure variation across the continuous reactor can be significant.

The unsteady state mass balance for aqueous species  $i$  in the packed bed and bubble column layers is:

$$\varepsilon_L \frac{\partial}{\partial t} c_i - \varepsilon_L E_L \nabla^2 c_i + u_L \nabla \cdot c_i = r_i \quad (2)$$

where  $\varepsilon_L$  is the liquid holdup, defined as the volume fraction of either the packed bed layer or bubble column layer occupied by the liquid phase,  $E_L$  (m<sup>2</sup> s<sup>-1</sup>) is the hydrodynamic dispersion coefficient,  $u_L$  (m s<sup>-1</sup>) is the superficial liquid velocity (which equals to zero for the experimental reactor),  $c_i$  (mol m<sup>-3</sup>) is the concentration of species  $i$  in the liquid phase, and  $r_i$  (mol m<sup>-3</sup> s<sup>-1</sup>) is the source term of species  $i$ . The aqueous species include CO<sub>2(aq)</sub>, Ca<sup>2+</sup> and total carbon ions (TCI) defined as the sum of HCO<sub>3</sub><sup>-</sup> and CO<sub>3</sub><sup>2-</sup>.

The gas chamber in the upper section of the experimental reactor serves as a reservoir of the initially supplied CO<sub>2</sub> and is modelled as a well-mixed container with gas entering from the top of the bubble column layer, and leaving through an outlet, recycling to the bottom of the reactor. Mass transfer of CO<sub>2</sub> from the headspace gas to the liquid phase through the top surface of the bubble column layer is found to be potentially significant for the experimental apparatus and is therefore modelled.

The boundary condition of [Eq. \(1\)](#) is:

$$\text{at gas inlet, } x = 0, \quad c_{CO_2(g)} = c_{CO_2(g),inlet} \quad (3)$$

The Danckwerts' boundary conditions [\[13\]](#) are adopted for [Eq. \(2\)](#):

$$\text{at liquid inlet: } x = H_{bed}, \quad u_L c_{i,inlet} = u_L c_i - D_{L,i} \nabla c_i \quad (4)$$

$$\text{at liquid outlet: } x = 0, \quad \nabla c_i = 0 \quad (5)$$

The subscript  $i$  represents the aqueous species, e. g. CO<sub>2(aq)</sub>, Ca<sup>2+</sup> and TCI. The mass conservation equation for the gas chamber (relevant for the experimental reactor) can be found in [Section S2.3](#) of SI.

### 2.2.2 Reaction kinetics

The aqueous-phase reactions involved in the model are as follows [\[14, 15\]](#).



Following [\[15\]](#), dissolution of calcite is assumed to occur by water attacking the mineral surface:



The following equation is adopted for calcite dissolution rate ( $r_{Ca^{2+}}$ , mol m<sup>-3</sup> s<sup>-1</sup>) which combines the impact of saturation [\[16\]](#) and pH:



$$r_{Ca^{2+}} = a_w^{pbl} [k_{H^+} c_{H^+} + k_{diss} (1 - \Omega)^n] \quad (11)$$

where  $a_w^{pbl}$  is the specific reactive solid surface area of the packed bed layer ( $m^{-1}$ ),  $k_{H^+}$  is a constant ( $m s^{-1}$ ) associated with  $c_{H^+}$ , the concentration of proton ( $mol m^{-3}$ ),  $k_{diss}$  ( $mol cm^{-2} s^{-1}$ ) is the surface area normalized calcite dissolution rate constant,  $n$  is an exponential constant (details can be found in [Section S2.4](#) of SI),  $\Omega$  is the level of saturation, defined as the ratio of  $Ca^{2+}$  and  $CO_3^{2-}$  concentrations with respect to the equilibrium constant:

$$\Omega = (c_{Ca^{2+}} c_{CO_3^{2-}}) / K_C \quad (12)$$

$a_w^{pbl}$  is essentially the specific surface area of particles:

$$a_w^{pbl} = 6(1 - \varepsilon_M) / d_p \quad (13)$$

where  $d_p$  (m) is the particle diameter,  $\varepsilon_M$  (-) is the porosity of packed bed layer, expressed as a function of particle size:

$$\varepsilon_M = 0.390 + \frac{1.740}{(d_R / d_p + 1.14)^2} \quad (14)$$

where  $d_R$  (m) is the diameter of the reactor.

Reactions (6) and (9) are modelled kinetically, and the following source terms for  $CO_2(aq)$  and TCI are obtained:

$$r_{CO_2(aq)} = r_{G-L} + \varepsilon_L (k_{12} c_{HCO_3^-} - k_{11} c_{CO_2(aq)} c_{OH^-} + k_{42} c_{HCO_3^-} c_{H^+} - k_{41} c_{CO_2(aq)}) \quad (15)$$

$$r_{TCI} = -\varepsilon_L (k_{12} c_{HCO_3^-} - k_{11} c_{CO_2(aq)} c_{OH^-} + k_{42} c_{HCO_3^-} c_{H^+} - k_{41} c_{CO_2(aq)}) + r_{Ca^{2+}} \quad (16)$$

Reactions (7) and (8) are assumed to remain in equilibrium and are modelled by:

$$c_{CO_3^{2-}} = K_2 c_{HCO_3^-} c_{OH^-} \quad (17)$$

$$K_3 c_{H^+} c_{OH^-} = 1 \quad (18)$$

To resolve  $c_{CO_3^{2-}}$ ,  $c_{HCO_3^-}$  and  $pH$ , the above two algebraic equations are solved together with Eq. (6) and a charge balance equation:

$$(c_{H^+} + 2c_{Ca^{2+}}) - (2c_{CO_3^{2-}} + c_{HCO_3^-} + c_{OH^-}) + \delta = 0 \quad (19)$$

where  $\delta$  represents the net charge brought into the reactor by the “inert” cations and anions contained in the seawater not participating to the modelled chemical reactions:

$$\delta = (2c_{CO_3^{2-},seawater} + c_{HCO_3^-,seawater} + c_{OH^-,seawater}) - (c_{H^+,seawater} + 2c_{Ca^{2+},seawater}) \quad (20)$$

The values of rate and equilibrium constants are listed in Table 1.

*Table 1. Rate constants and equilibrium constants*

Parameter	Value	Unit	Reference
$K_1$	$K_4/K_w$	$m^3 \text{ mol}^{-1}$	Calculated
$K_2$	$10^{(1394.7/T+4.777-0.0184S+0.000118S^2)}/K_w$	$m^3 \text{ mol}^{-1}$	43
$K_3$	$1/K_w$	$m^6 \text{ mol}^{-2}$	Calculated
$K_4$	$\rho_L \exp^{[2.83655-2307.1266/T-1.5529413\ln(T)-(0.20760841+4.40484/T)S^{0.5}+0.08468345S-0.00654208S^{1.5}]}$	$\text{mol m}^{-3}$	44
$K_5$	$K_C/(K_2 K_w)$	$\text{mol m}^{-3}$	Calculated
$K_6$	$K_4 K_C/(K_2 K_w)$	$\text{mol}^2 \text{ m}^{-6}$	Calculated
$K_C$	$10^{[-171.9065+0.077993T-2839.319/T-71.595\ln T+(0.77712-0.0028426T-178.34/T)S^{0.5}+0.07711S-0.0041249S^{1.5}]}$	$\text{mol}^2 \text{ L}^{-2}$	44
$K_w$	$\rho_L^2 10^{[148.9802-13847.26/T-23.6521\ln T+(118.67/T+1.0495\ln T-5.977)S^{0.5}-0.01615S]}$	$\text{mol}^2 \text{ m}^{-6}$	44
$k_{11}$	$\exp^{[-930.13+0.115^{0.5}+3.1\times 10^4/T+140.9\ln T]}/K_w$	$\text{L mol}^{-1} \text{ s}^{-1}$	45
$k_{41}$	$\exp^{(1246.98-6.19\times 10^4/T-183.0\ln T)}$	$\text{s}^{-1}$	45
$k_{51}$	$10^{(0.198-444/T)}$	$\text{cm s}^{-1}$	46

Note: S is salinity, set to a representative value of 35 for seawater.

### 2.2.3 Mass transfer, interfacial areas and phase fractions

In Eq. (1),  $r_{G-L}$  ( $\text{mol m}^3 \text{ s}^{-1}$ ) is the source term for the mass transfer of  $\text{CO}_2$  from the gas flow into the aqueous phase:

$$r_{G-L} = a_{G-L} k_L (c_{CO_2(aq)}^* - c_{CO_2(aq)}) \quad (21)$$

where  $a_{G-L}$  ( $\text{m}^{-1}$ ) is the gas-liquid interfacial area per unit volume and  $k_L$  ( $\text{m s}^{-1}$ ) is the liquid phase mass transfer coefficient (mass transfer resistance on the gas side is omitted). The saturated concentration of  $\text{CO}_2$  in the liquid phase,  $c_{\text{CO}_2(aq)}^*$  ( $\text{mol m}^{-3}$ ), is calculated by Henry's law (Section S2.5 of SI).

The interfacial area for mass transfer depends on the bubble diameter ( $d_b$ ) and gas holdup:

$$a_{G-L} = 6\varepsilon_G/d_b \quad (22)$$

For the bubble column layer, the equations of Akita and Yoshida [17] were used to estimate  $\varepsilon_G$ ,  $d_b$  and  $k_L$ . In the packed bed layer, the same source was used to estimate  $d_b$  but for  $\varepsilon_G$ , the work by Maldonado et al. [18] and Taghavi et al. [19] was followed, which considers separate contributions from a static component as a function of solid particle size (accounting for the gas initially trapped by the particles) and a dynamic component (accounting for the influence of gas velocity).

It is worth noting that the packed bed layer is a three-phase domain, and the bubble column layer (relevant only for the experimental reactor) is a two-phase domain without a solid phase. Thus, the following equations hold:

$$\varepsilon_S^{pbl} + \varepsilon_L^{pbl} + \varepsilon_G^{pbl} = 1 \quad (23)$$

$$\varepsilon_L^{bcl} + \varepsilon_G^{bcl} = 1 \quad (24)$$

The subscript  $S$ ,  $L$  and  $G$  represent solid, liquid and gas phase, the superscript  $pbl$  and  $bcl$  represent packed bed layer and bubble column layer, respectively.

The volume fraction of solid particles in the packed bed layer  $\varepsilon_S^{pbl}$  is equal to  $1 - \varepsilon_M$ . The gas holdup of the bubble column layer is expressed as [17, 20]:

$$\varepsilon_L^{bcl} = \frac{1}{8} \ln[1 + 8Cg^{-7/24} (\frac{\mu_L}{\rho_L})^{-1/6} (\frac{\sigma_L}{\rho_L})^{-1/8} u_G] \quad (25)$$

where  $\mu_L$  (Pa s),  $\rho_L$  (kg m<sup>-3</sup>) and  $\sigma_L$  (N m<sup>-1</sup>) are the viscosity, density and surface tension of liquid,  $u_G$  (m s<sup>-1</sup>) is the superficial gas velocity, and the constant  $C = 0.25$  when the liquid is an aqueous solution of electrolytes.

By considering the population of bubbles in the packed bed layer as some that are captured by the solids as static hold-up (having zero velocity) and some that are rising (which provide dynamic hold-up), the total gas hold-up is given by [18, 21]:

$$\varepsilon_G^{pbl} = \varepsilon_{G,static}^{pbl} + \varepsilon_{G,dyn}^{pbl} \quad (26)$$

There is evidence from these studies that the dynamic hold-up plays a decreasing role as gas velocity increases, and the rising bubbles interact more frequently with those that are captured. To allow for the interaction of the two types of holdups we propose:

$$\varepsilon_{G,static}^{pbl} = \varepsilon_{G,static,0}^{pbl} \cdot \exp\left(-\frac{\varepsilon_{G,dyn}^{pbl}}{\varepsilon_{G,static,0}^{pbl}}\right) \quad (27)$$

There is also evidence that  $\varepsilon_{G,static,0}^{pbl}$  attains its maximum value for a certain particle size [19]. In our system we model this by the dimensional equation:

$$\varepsilon_{G,static,0}^{pbl} = 0.055 \exp\left[-0.9(\sqrt{d_p} - 1.7)^2\right] \quad (28)$$

where  $d_p$  is the solid particle diameter (mm).

$$\varepsilon_{G,dyn}^{pbl} = u_G / u_{b,0} \quad (29)$$

where  $u_{b,0}$  (m s<sup>-1</sup>) is the bubble rising velocity, for which a typical value of 0.3 m s<sup>-1</sup> is adopted, consistent with the above hold-up data.

In Eq. (22), the bubble diameter in the packed bed layer and bubble column layer is calculate by Akita and Yoshida [17]:

$$d_b = 26d_R Bo_L^{-0.50} Ga_L^{-0.12} Fr_G^{-0.12} \quad (30)$$

where  $d_R$  (m) is the column diameter,  $Fr_G$  is the Froude number of the gas phase,  $Bo_L$  and  $Ga_L$  are Bond number and Froude number of the liquid, respectively.

$$Bo_L = \frac{gd_R^2 \rho_L}{\sigma_L}, \quad Ga_L = \frac{g \rho_L^2 d_R^3}{\mu_L^2}, \quad Fr_G = \frac{u_G}{(gd_R)^{0.5}} \quad (31)$$

As Eq. (30) was originally developed for solid-free bubble columns, the gas and liquid superficial velocities for the packed bed layer are converted to become superficial velocities with respect to the cross-sectional area of the void space (as opposed to that of the reactor) for being used in Eq. (30):

$$u_G^{bcl} = u_G \mathcal{E}_M, \quad u_L^{bcl} = u_L \mathcal{E}_M \quad (32a,b)$$

For  $k_L$  in the packed bed layer, the modelling is based on the surface renewal theory of Danckwerts [22], which is also adopted to model the mass transfer at the top surface of the bubble column layer in the experimental reactor (Section S2.5 of SI). When the mass transport resistance on the gas side is neglected, the overall mass transport coefficient for the transfer of carbon dioxide in the bubble column layer is calculated from the following expression [17]:

$$k_L^{bcl} = 0.5 g^{5/8} (D_L d_b^{bcl})^{1/2} (\sigma_L / \rho_L)^{-3/8} \quad (33)$$

where  $D_L$  ( $\text{m}^2 \text{s}^{-1}$ ) is the molecular diffusivity of aqueous  $\text{CO}_2$  (values see Table S4 in SI), and  $d_b^{bcl}$  (m) is the bubble diameter in the bubble column layer.

In the packed bed layer, Danckwerts [22] showed that transfer by diffusion into a liquid surface with a uniform rate of surface renewal gives rise to a liquid-phase mass transfer coefficient given by:

$$k_L^{pbl} = \sqrt{D_L u_s / d_b^{pbl}} \quad (34)$$

where  $d_b^{pbl}$  (m) is the bubble diameter in the packed bed layer,  $u_s$  ( $\text{m s}^{-1}$ ) is the mean slip velocity, expressed as:

$$u_s = \left( \frac{\mathcal{E}_{G,static}^{pbl}}{u_G} + \frac{1}{u_{b,0}} \right)^{-1} \quad (35)$$

As expected from the above equation, the mean slip velocity approaches zero as  $u_G \rightarrow 0$ , and approaches  $u_{b,0}$  as  $u_G$  increases.

Calculation of the longitudinal dispersion coefficient ( $E_L$ ) is based on Darton [20]. In the conservation equation of mass, the longitudinal dispersion coefficient is calculated from the following empirical correlation [20]:

$$E_L = 0.35d_e^{4/3}(u_G g)^{1/3} \quad (36)$$

where  $d_e$  (m) is set to the particle diameter  $d_p$  for the packed bed layer and to the reactor diameter  $d_R$  for the bubble column layer.

#### 2.2.4 Particle shrinkage and bed height change

The total loss rate of the solid mass, particle diameter change rate, the height change rates of packed bed layer and bubble column layer, are calculated by the following expressions.

$$\frac{dm_p}{dt} = -M_p \cdot r_{Ca^{2+}}^{ave} \cdot V^{pbl} \quad (37)$$

$$\frac{dd_p}{dt} = -\frac{1}{6} \frac{M_p \cdot r_{Ca^{2+}}}{\rho_p \varepsilon_S^{pbl}} d_p \quad (38)$$

$$\frac{dH^{pbl}}{dt} = -\frac{m_p^0 M_p \cdot r_{Ca^{2+}}}{S_R \rho_p^2 (\varepsilon_S^{pbl})^2} \left(\frac{d_p}{d_p^0}\right)^3 \quad (39)$$

$$\frac{dH^{bcl}}{dt} = \varepsilon_L^{pbl} \frac{dH_t^{pbl}}{dt} \quad (40)$$

where  $r_{Ca^{2+}}^{ave}$  ( $\text{mol m}^{-3} \text{s}^{-1}$ ) is the weathering reaction rate averaged across the packed bed layer,  $M_p$  ( $\text{kg mol}^{-1}$ ) is the molar mass of the solid particles,  $V^{pbl}$  ( $\text{m}^3$ ) is the volume of the packed bed layer,  $\rho_p$  ( $\text{kg m}^{-3}$ ) is particle density,  $m_p^0$  (kg) is the initial particle mass,  $d_p^0$  (m) is the initial particle diameter,  $\varepsilon_S^{pbl}$  is the volume fraction of solid particles in the packed bed layer.

The rate of change of particle diameter, packed bed layer height and bubble column layer height are obtained from the relationship between mass, volume and diameter of particles. The change of the total height of the reaction volume can thus be obtained to determine the adjustment of the computational domain and reflects the decrease in reaction volume owing to particle dissolution. Detailed derivation of equations for particle shrinkage and computational domain change can be found in [Section S2.6](#) of SI.

## 2.3 Quantifying energy consumption

Energy consumption comprises the following three components.

### 2.3.1 Energy for maintaining gas and liquid flow

Gas flowing through the reactor must overcome a pressure drop by action of a blower or compressor. The mechanical energy input to this device, i.e. the compression work, over a time period  $t$ , is

$$W_G = \frac{1}{\eta} \int_0^t \left\{ p_{in} Q_G^{in} \frac{\gamma}{\gamma - 1} \left[ \left( \frac{p_{out}}{p_{in}} \right)^{(1-1/\gamma)} - 1 \right] \right\} dt \quad (41)$$

where  $\eta$  is compressor efficiency, assumed to be 0.8.  $\gamma$  is the ratio of the specific heats at constant pressure and constant volume,  $Q_G^{in}$  ( $\text{m}^3 \text{s}^{-1}$ ) is the inlet volumetric flow rate of gas,  $p_{in}$  (Pa) is the pressure of the feed stream prior to compression, and  $p_{out}$  (Pa) is the outlet pressure of the compressor, i.e. the pressure at the bottom entrance of the reactor. The calculation of pressure drop, which determines  $p_{out}$ , could be found in [Section S2.7](#) of SI.

The required mechanical energy for pumping water to the height of the packed bed is calculated by:

$$W_L = \frac{1}{\eta} \int_0^t \rho_L Q_L g H^{pbl} dt \quad (42)$$

where  $Q_L$  ( $\text{m}^3 \text{s}^{-1}$ ) is the volumetric flow rate of liquid, the efficiency  $\eta$  is again taken as 0.8.

The total energy consumption for maintaining gas and liquid flows is thus

$$E_{pump} = W_G + W_L \quad (43)$$

### 2.3.2 Energy consumption for CO<sub>2</sub> enrichment

Existing, experimentally demonstrated systems that directly capture CO<sub>2</sub> from the atmosphere (known as Direct Air Capture or DAC) are all for producing high-purity CO<sub>2</sub> [23]. Theoretically, a DAC process producing a lower purity of CO<sub>2</sub> would require less energy input [24, 25]; possible schemes for such processes include adsorption-based DAC with regeneration using air (as opposed to steam) [26] and membrane-based DAC [27]. However, there is currently a lack of reliable data of the attainable performance of air-CO<sub>2</sub> enrichment processes aiming at low CO<sub>2</sub> purity, therefore we estimated the energy requirement as follows. The theoretical minimum work required for concentrating both the fresh (top-up) ambient air flow and the recycled gas stream to the specified feed CO<sub>2</sub> concentration is first calculated based on the change in Gibbs free energy. Darton and Yang [24] found the actual requirement for thermal energy (based mainly on data for flue gas scrubbing using absorption processes) to be a factor approximately 14 greater. If applied to a DAC process for producing pure CO<sub>2</sub>, this factor predicts thermal energy consumption to be ~7.3 MJ/kg CO<sub>2</sub>, which falls into the mid-range of what was recently reported of solid sorbent-based processes (~4-12 MJ/kg CO<sub>2</sub> [23]) and is adopted here. Further, a heat pump-based solution is assumed to provide the thermal energy at a supply temperature around 100 °C, typical of the regeneration operating temperature of recently reported DAC processes based on temperature swing [28]. At such temperature levels, a Coefficient of Performance (COP) of 2.5 is within the range achievable by heat pumps for industrial heating [29, 30]. These considerations allow us to estimate the total electrical energy required for preparing the feed gas to the reactor at the specified CO<sub>2</sub> concentration, described below.

The theoretical minimum work,  $W_1$  (W), required for concentrating the outlet gas stream with CO<sub>2</sub> mole fraction of  $x_{CO_2}^{outlet}$  back to the concentration at the inlet  $x_{CO_2}^{inlet}$ , assuming 100% recovery of CO<sub>2</sub>, can be calculated by the following expression [24]:

$$W_1 = \int_0^t RT \left[ \ln\left(\frac{x_{CO_2}^{inlet}}{x_{CO_2}^{outlet}}\right)n_{CO_2}^{recover} + \ln\left(\frac{x_{inert}^{inlet}}{x_{inert}^{outlet}}\right)n_{inert}^{recover} + \ln\left(\frac{1}{x_{inert}^{outlet}}\right)n_{inert}^{reject1} \right] dt \quad (44)$$



where  $x_{CO_2}^{inlet}$  and  $x_{inert}^{inlet}$  are the mole fractions of CO<sub>2</sub> and inert gas at the inlet of the reactor,  $x_{CO_2}^{outlet}$  and  $x_{inert}^{outlet}$  are the mole fractions of CO<sub>2</sub> and inert gas at the outlet of the reactor,  $n_{CO_2}^{recover}$ ,  $n_{inert}^{recover}$  and  $n_{inert}^{reject1}$  (mol s<sup>-1</sup>) are the molar flow rates of recovered CO<sub>2</sub>, recovered inert gas and rejected inert gas, respectively. Due to the consumption of CO<sub>2</sub> during the EW process, a certain amount of CO<sub>2</sub> must be replenished from the atmosphere as top-up to the CO<sub>2</sub> recycled (and enriched) from the reactor outlet, to maintain constant CO<sub>2</sub> concentration and volumetric flowrate of the gas feed to the reactor. The theoretical minimum work required for concentrating atmospheric air,  $W_2$  (J), can be calculated by the same principle as for the recycled gas:

$$W_2 = \int_0^t RT \left[ \ln\left(\frac{x_{CO_2}^{inlet}}{x_{CO_2}^{air}}\right)n_{CO_2}^{top-up} + \ln\left(\frac{x_{inert}^{inlet}}{x_{inert}^{air}}\right)n_{inert}^{top-up} + \ln\left(\frac{1}{x_{inert}^{air}}\right)n_{inert}^{reject2} \right] dt \quad (45)$$

where  $x_{CO_2}^{air}$  is the CO<sub>2</sub> mole fraction in atmosphere (410 ppm),  $x_{inert}^{air}$  is the mole fraction of inert gas in atmosphere,  $n_{CO_2}^{top-up}$  and  $n_{inert}^{top-up}$  (mol s<sup>-1</sup>) are the molar flow rate of CO<sub>2</sub> and that of the inert gas in the top-up stream to become part of the feed gas to the reactor,  $n_{inert}^{reject2}$  is the molar flow rate of the inert rejected by the process that produces the top-up stream with enriched CO<sub>2</sub>.

In Eq. (45),  $x_{CO_2}^{inlet}$  is a pre-defined parameter, while  $x_{CO_2}^{outlet}$  in Eq. (44) is calculated by the model. Note that in any gas flow, the sum of CO<sub>2</sub> mole fraction and inert gas mole fraction is unity. All the molar flow rate terms can readily be derived from the specified volumetric flowrate of the gas flow and mass balance.

The total electrical energy required for preparing the feed gas per kg CO<sub>2</sub> capture,  $E_{feed}$  (J kg<sup>-1</sup>) is

$$E_{feed} = \zeta(W_1 + W_2) \quad (46)$$

where the conversion ratio  $\zeta = 14/2.5$ , according to the approach explained above.

### 2.3.3 Energy consumption for supplying mineral particles

Excavation, drilling, blasting and short-range hauling for a range of ores and rocks typically range between 12.5 and 96.7 MJ t<sup>-1</sup> [31-34]. Following the work of Renforth et al. [34], a value of  $E_{other} = 20$  MJ t<sup>-1</sup> was

chosen for this work, all energy regarded as electricity. This is further combined with the grinding energy for producing particles of specific sizes (diameters), calculated using Bond's law parameterised with data for calcite [35]. When the initial size of particle is assumed as effectively infinite, the required energy for grinding is given as follows [36]:

$$E_{grinding} = 0.01W_i \left( \frac{1}{\sqrt{d_p}} \right) \quad (47)$$

where  $d_p$  is the produced particle diameter (in m);  $W_i$  is the working index, which is equal to  $4.176 \times 10^4$  J  $\text{kg}^{-1}$  for calcite.

## 2.4 Numerical solution method

The numerical solution of the fully coupled governing equations was based on the finite element method (FEM) implemented in commercial software COMSOL Multiphysics 5.4. The “extremely fine” meshing option was chosen. The MUMPS time-dependent solver was adopted with default parameters settings and the computational tolerance was set to be physics-controlled with a relative tolerance of 0.01.

## 3. Results and discussion

### 3.1 Model validation

The experimental reactor model was used to predict the outcome of 12 sets of experiments in which the change of the  $\text{CO}_2$  concentration in the gas chamber was monitored as described in Section 2.1 and shown in Fig. 3. The rate of absorption decreases as time passes and the back pressure of  $\text{CO}_2$  above the liquor increases. The agreement between experiment and simulation shown in Fig. 3 is fair, though with several runs at the lower (5%) initial  $\text{CO}_2$  concentration the initial rate of absorption is underestimated (Fig. 3a and 3b). This is not seen in all runs, nor at the higher (50%) initial concentration. We note that the prediction involves many physical and chemical processes, using basic data and empirical correlations from the literature and a novel correlation scheme - Eqs (23) and (26) to (29) - for hold-ups in the packed bed layer also based on literature measurements. None of the parameters used in our simulation was tuned for the experiments reported here. We therefore consider the agreement between model and experiment displayed

here to offer a satisfactory validation of the experimental reactor model. This in turn supports the use of the continuous reactor model for further preliminary simulation analysis as it shares the same core content (mass transfer, hold-up and bubble characteristics, reaction kinetics and equilibria). Naturally further experimental verification would be highly desirable.

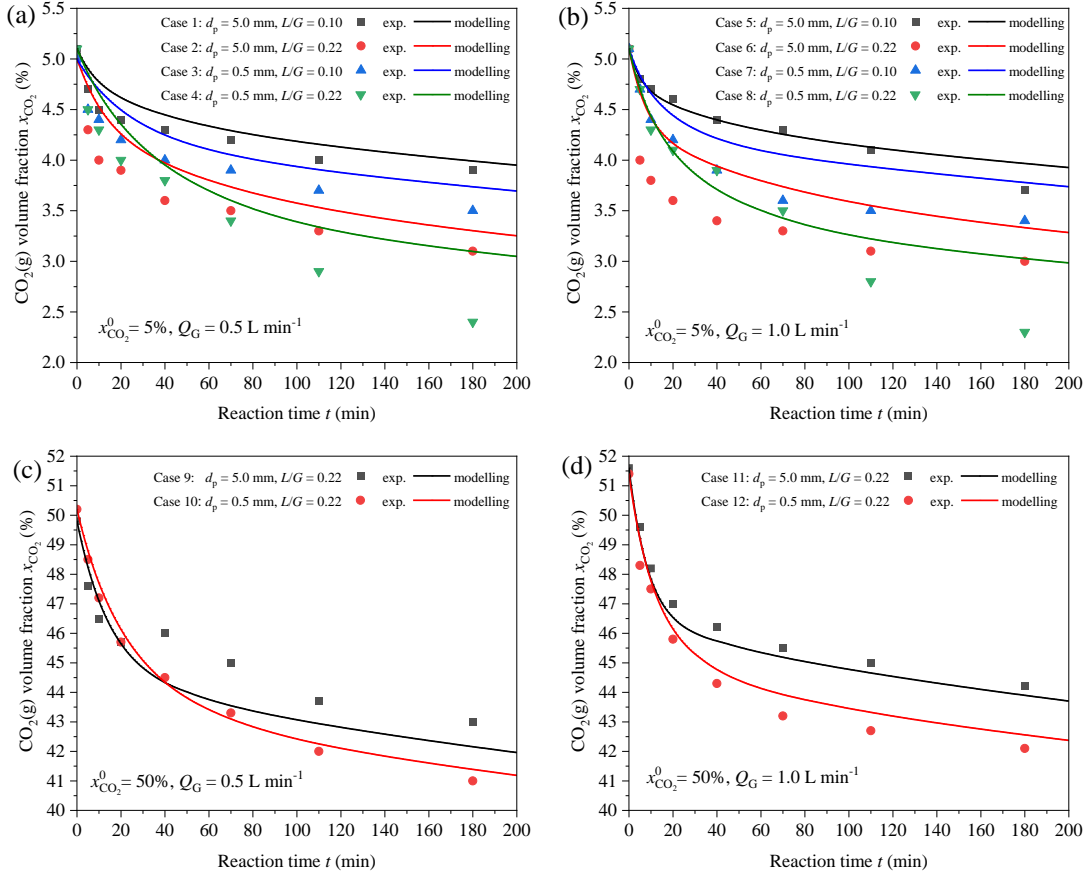


Fig. 3. Results of model validation. Subfigures (a), (b), (c) and (d) are for different initial  $\text{CO}_2$  concentration and  $Q_G$ .  $L/G$  is the ratio of liquid to gas volume in the reactor.

### 3.2 Simulation assessment of up-scaled continuous operations

Two sets of simulation studies were carried out to assess the performance of the continuous reactor with a diameter of 1 m under a range of parametric settings as shown in Table 2. The first set, referred to as “main cases”, setting the concentration of  $\text{CO}_2$  in the gas feed to 1% as a modest elevation above atmospheric concentration yet allowing the weathering of calcite to occur in seawater, assessed the impact of four parameters: particle diameter ( $d_p$ ), bed height ( $H_{bed}$ ), and gas ( $u_G$ ) and liquid ( $u_L$ ) superficial velocities. The

impact of each parameter was studied by a dedicated simulation case. Each case further contains 8 sub-cases to simulate combinations of the values of the other three (3) parameters set to their two (2) limits. Additionally, a set of “extra cases” were simulated, to evaluate the reactor at further elevated CO<sub>2</sub> concentrations; a range of values for  $H_{bed}$ , a parameter shown to be particularly significant in preliminary tests, were also considered while other parameters were fixed.

Table 2. Parametric settings for the simulation of the continuous reactor

Common parameters		Value
Operating temperature ( $T$ ) and pressure ( $P$ )		20 °C, 1atm
Diameter of reactor column ( $d_R$ , m)		1.0
Parameters tested, <b>main cases</b>	Lower limit	Upper limit
Gaseous CO <sub>2</sub> feed mole fraction ( $x_{CO_2}^{inlet}$ )		1%
Particle diameter ( $d_p$ , mm)	1.0	10
Bed height ( $H_{bed}$ , m)	0.2	10
Gas superficial velocity ( $u_G$ , m s <sup>-1</sup> )	$1 \times 10^{-4}$	$1 \times 10^{-3}$
Liquid superficial velocity ( $u_L$ , m s <sup>-1</sup> )	$1 \times 10^{-5}$	$1 \times 10^{-4}$
Parameters tested, <b>extra cases</b>		Value
Gaseous CO <sub>2</sub> feed mole fraction ( $x_{CO_2}^{inlet}$ )	0.01	0.1
Particle diameter ( $d_p$ , mm)		5.0
Bed height ( $H_{bed}$ , m)	0.2	5
Gas superficial velocity ( $u_G$ , m s <sup>-1</sup> )		$1 \times 10^{-4}$
Liquid superficial velocity ( $u_L$ , m s <sup>-1</sup> )		$5 \times 10^{-5}$

### 3.2.1 Impact of key process parameters

Among the four parameters evaluated in the main cases, the impact of  $d_p$  on the CO<sub>2</sub> capture rate (CCR) and specific energy consumption (SEC) (Fig. 4 a-b, where only results with  $H_{bed} = 0.2$  m are shown for clarity) appeared to be slight within the tested range (1 mm – 10 mm), despite its direct influence on the reactive surface area of the solid particles. This is in accordance with the findings of our previous work on calcite weathering in a trickle bed reactor [11] where it was shown that the rate was largely controlled by gas-to-liquid mass transfer. It is worth noting that larger  $d_p$  would mean lower energy cost for supplying

particles (cf. Eq. 47) which, however, represents only a small fraction of the total energy demand (usually less than 5%, cf. Table 3). Since particle diameter had little overall effect, only cases with  $d_p = 1$  mm are shown in Fig. 4 c-d and Fig. 5 demonstrating the more significant impacts of bed height and fluid velocities. Increasing  $H_{\text{bed}}$  generally improves CCR, which is most significant with the greatest  $u_G$  and  $u_L$  as these conditions make “fuller” use of the extra height (Fig. 4 c-d). However, the impact of  $H_{\text{bed}}$  tends to diminish beyond a certain level, particularly at low  $u_G$  and  $u_L$ , as significant further mass transfer can no longer be achieved by a greater height. SEC, on the other hand, is greater in taller beds, suggesting that within the tested range, the benefit of improved CO<sub>2</sub> capture by additional bed height is outweighed by the increase in the energy burden for maintaining the gas and liquid flows in taller beds. Performance is the poorest in cases combining the greatest  $u_G$  with the lowest  $u_L$ , as they entail a high energy consumption (due to the compression work for the large gas flow) but only provide limited CCR since the small liquid flow quickly becomes saturated.

To a large extent, the impact of the superficial gas velocity ( $u_G$ ) in Fig. 5 a-b is similar to that of  $H_{\text{bed}}$ : increase in  $u_G$  improves CCR and SEC, with the impact subsequently diminishing; on SEC, greater  $u_G$  would lead to higher consumption, suggesting that the gain in CCR is outweighed by the energy burden for overcoming greater pressure drop. The latter is particularly visible in the cases with highest  $H_{\text{bed}}$  and lowest  $u_L$  since these incur a high energy burden due to pressure drop, whilst the small liquid flow easily becomes saturated. In contrast,  $u_L$  shows rather different impacts (Fig. 5 c-d). Increasing  $u_L$  improves CCR, mainly through reduced saturation (lower  $c_{\text{CO}_2(\text{aq})}$ ) and thus a greater mass transfer driving force. This positive effect on CCR is seen to outweigh the increase in energy consumption for water pumping, leading to reduction in SEC.

Finally, the impact of feed CO<sub>2</sub> concentration (mole fraction,  $x_{\text{CO}_2}^{\text{inlet}}$ ) is revealed by results for the extra cases (Fig. 6). Regardless of the bed height, greater  $x_{\text{CO}_2}^{\text{inlet}}$  (within the tested range) always improves the gas-liquid mass transfer driving force and hence the CCR. On SEC, the effect is bed height dependent. This is due to the change in the relative importance of CO<sub>2</sub> enrichment (as a function of  $x_{\text{CO}_2}^{\text{inlet}}$ ) and gas and

liquid pumping (as a function of  $H_{\text{bed}}$ ) in total energy consumption: the former is relatively more important at lower  $H_{\text{bed}}$  where the pumping energy demand is low, and the latter becomes increasingly dominant at higher  $H_{\text{bed}}$ . Consequently, when  $H_{\text{bed}} = 0.2$  m,  $x_{\text{CO}_2}^{\text{inlet}} = 1\%$  results in the minimum SEC, whereas when  $H_{\text{bed}}$  is 5 m, SEC steadily reduces towards a minimum value as  $x_{\text{CO}_2}^{\text{inlet}}$  increases, at the fluid velocities shown here.

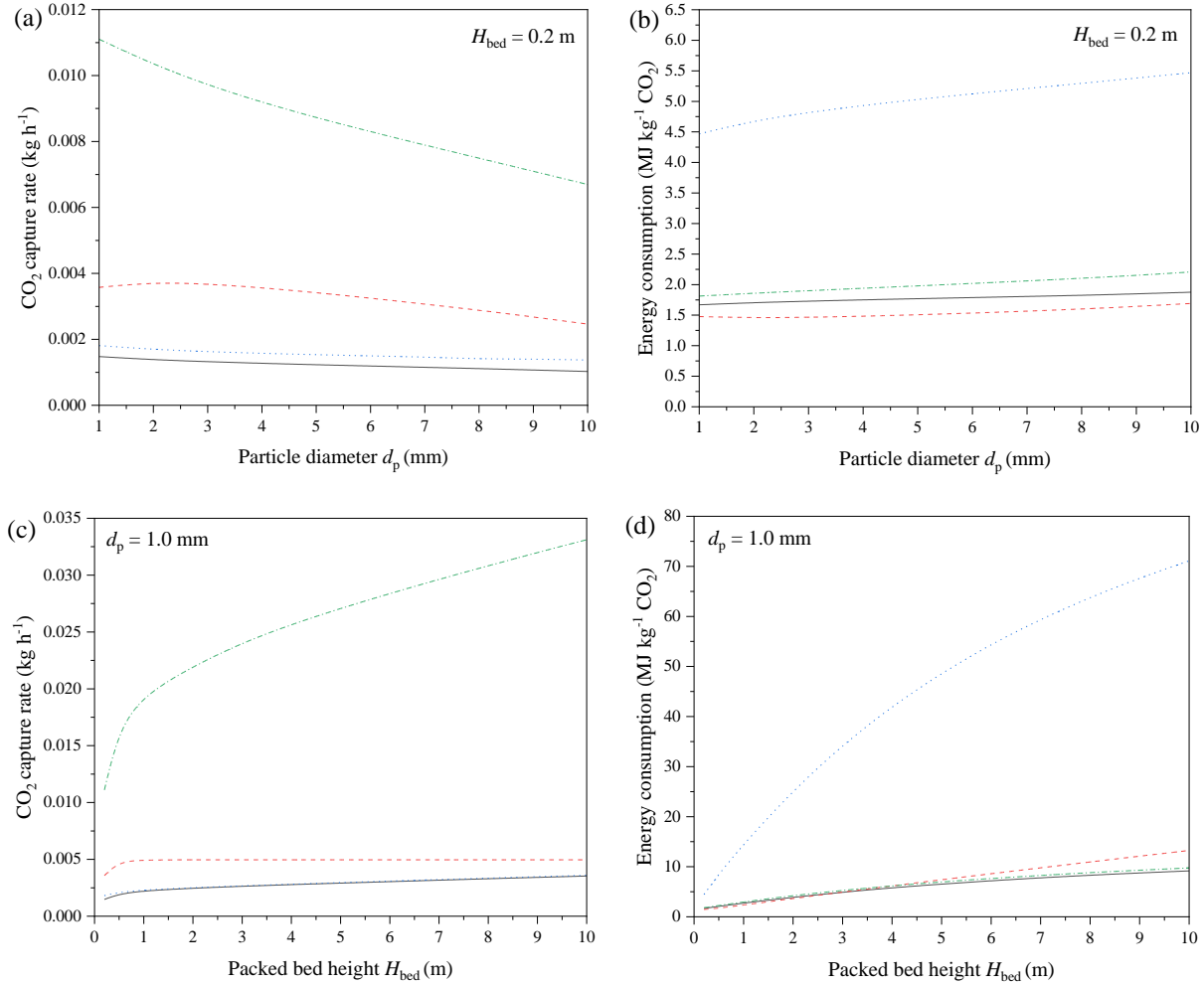


Fig. 4. Impact of particle size (a, b) and bed height (c, d) on  $\text{CO}_2$  capture rate (a, c) and specific energy consumption (b, d) at different gas and liquid superficial velocities. solid line -  $u_G = 1.0 \times 10^{-4} \text{ m s}^{-1}$ ,  $u_L = 1.0 \times 10^{-5} \text{ m s}^{-1}$ ; dash line -  $u_G = 1.0 \times 10^{-4} \text{ m s}^{-1}$ ,  $u_L = 1.0 \times 10^{-4} \text{ m s}^{-1}$ ; dot line -  $u_G = 1.0 \times 10^{-3} \text{ m s}^{-1}$ ,  $u_L = 1.0 \times 10^{-5} \text{ m s}^{-1}$ ; dash dot line -  $u_G = 1.0 \times 10^{-3} \text{ m s}^{-1}$ ,  $u_L = 1.0 \times 10^{-4} \text{ m s}^{-1}$ .

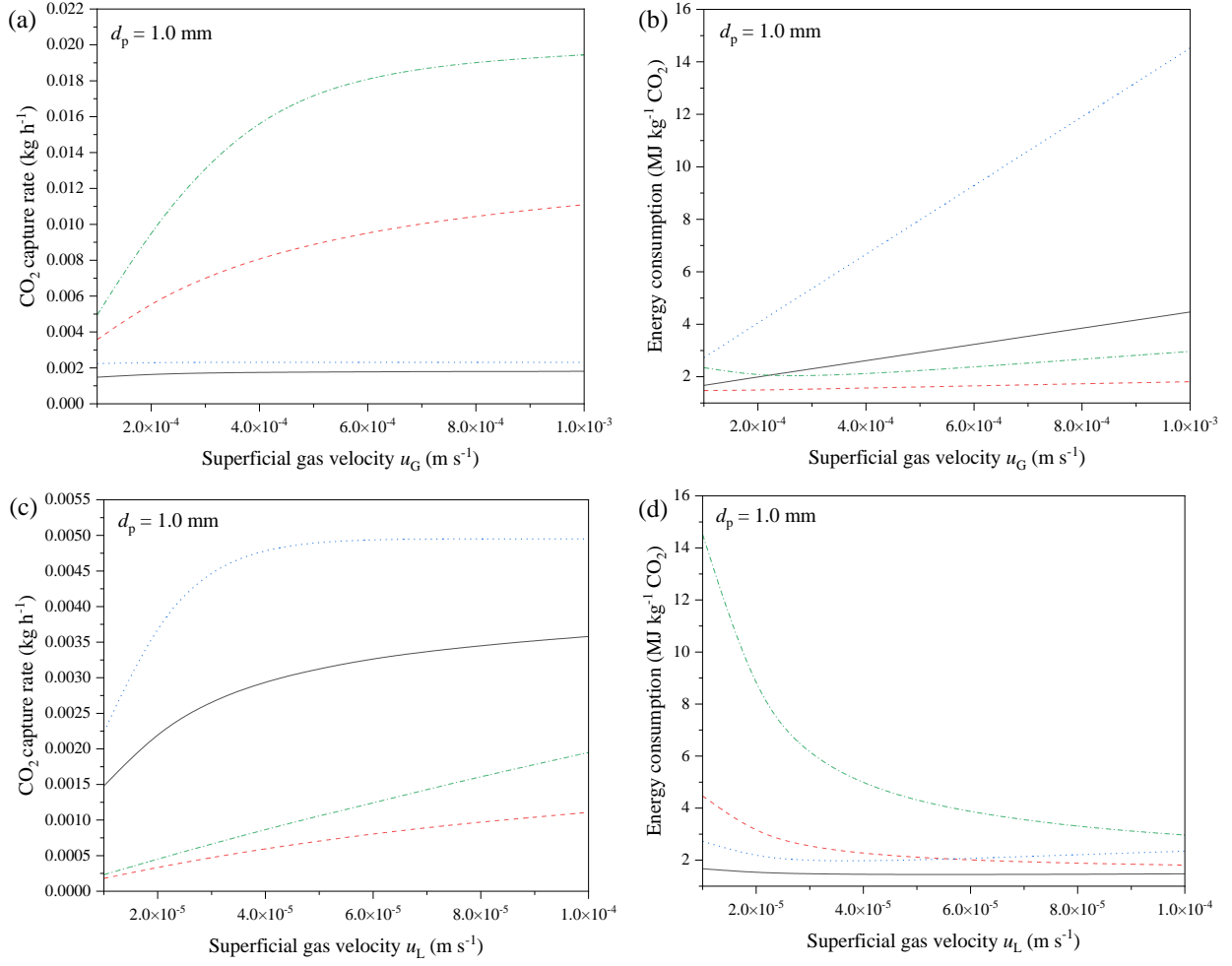


Fig. 5. Impact of superficial velocities of gas (a, b) and liquid (c, d) on  $\text{CO}_2$  capture rate (a, c) and specific energy consumption (b, d) at different bed heights. (a, b): solid line -  $H_{bed} = 0.2 \text{ m}$ ,  $u_L = 1.0 \times 10^{-5} \text{ m s}^{-1}$ ; dash line -  $H_{bed} = 0.2 \text{ m}$ ,  $u_L = 1.0 \times 10^{-4} \text{ m s}^{-1}$ ; dot line -  $H_{bed} = 1.0 \text{ m}$ ,  $u_L = 1.0 \times 10^{-5} \text{ m s}^{-1}$ ; dash dot line -  $H_{bed} = 1.0 \text{ m}$ ,  $u_L = 1.0 \times 10^{-4} \text{ m s}^{-1}$ ; (c, d): solid line -  $H_{bed} = 0.2 \text{ m}$ ,  $u_G = 1.0 \times 10^{-4} \text{ m s}^{-1}$ ; dash line -  $H_{bed} = 0.2 \text{ m}$ ,  $u_G = 1.0 \times 10^{-3} \text{ m s}^{-1}$ ; dot line -  $H_{bed} = 1.0 \text{ m}$ ,  $u_G = 1.0 \times 10^{-4} \text{ m s}^{-1}$ ; dash dot line -  $H_{bed} = 1.0 \text{ m}$ ,  $u_G = 1.0 \times 10^{-3} \text{ m s}^{-1}$ .

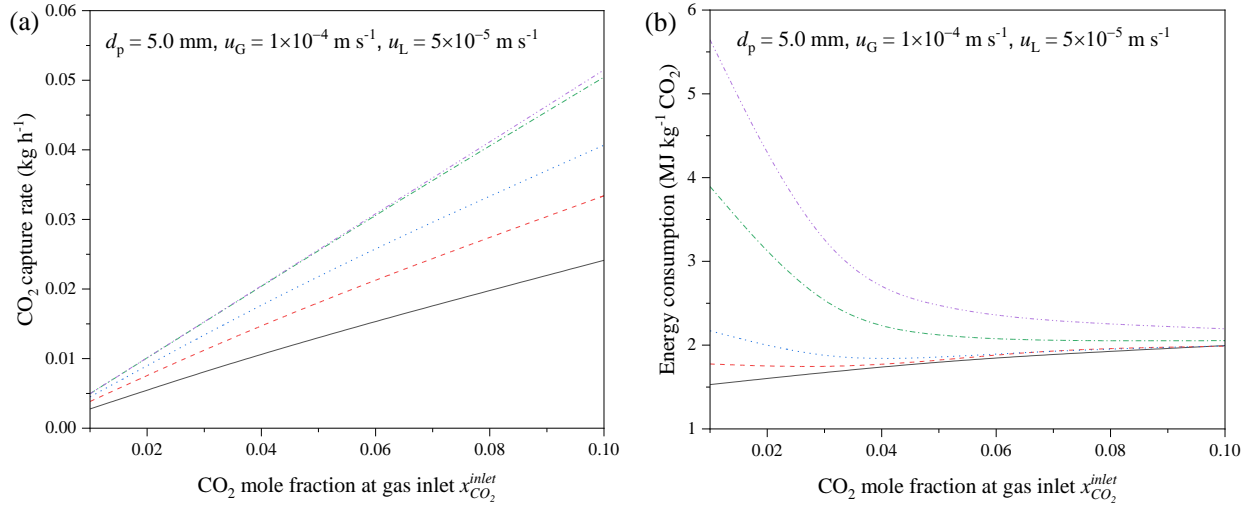


Fig. 6. Impact of inlet  $\text{CO}_2$  concentration on  $\text{CO}_2$  capture rate (a) and specific energy consumption (b) at different bed heights. solid line -  $H_{bed} = 0.2$  m; dash line -  $H_{bed} = 0.5$  m; dot line -  $H_{bed} = 1.0$  m; dash dot line -  $H_{bed} = 3.0$  m; dash dot dot line -  $H_{bed} = 5.0$  m.

### 3.2.2 Desirable parametric settings and attainable performance

Based on the simulation results of the main and extra cases, two key performance indicators, SEC (in  $\text{MJ kg}^{-1}$  or  $\text{GJ tonne}^{-1}$ ) and specific space requirement (SSR, in  $\text{m}^2 (\text{tonne year}^{-1})^{-1}$ ) can be assessed. The latter is proportional to ground area occupied by the reactor ( $S_R$ ) and inversely proportional to CCR:

$$SSR = \frac{S_R (\text{m}^2)}{\text{CO}_2 \text{ capture rate } (\text{kg h}^{-1}) \times 1 (\text{tonne}) / 1000 (\text{kg}) \times 8760 (\text{h}) / 1 (\text{year})} \quad (48)$$

Our calculations show that, in general, SEC and SSR are similarly affected by  $d_p$  (for both, the smaller  $d_p$ , the better, though the variation is slight) and  $u_L$  (for both, the larger the  $u_L$ , the better). But SEC and SSR follow opposite trends when  $u_G$  or  $H_{bed}$  changes. Further, SSR is positively correlated with  $x_{\text{CO}_2}^{\text{inlet}}$ , but the variation of SEC with  $x_{\text{CO}_2}^{\text{inlet}}$  is complex and dependent on  $H_{bed}$ . The above observations mean that trade-offs exist between SSR and SEC with respect to the selection of optimal parametric settings. Fig. 7 visualises the predicted SSR-SEC pairs extracted from the simulation results, where the favourable region lies in the lower left corner (see inset). Although rigorous optimisation of the parameters is beyond the scope of this work, the size of the simulated data set (336 points from the main cases, 35 points from the



extra cases) is adequate to derive two “empirical” Pareto fronts. One is based only on the main cases ( $x_{CO_2}^{inlet} = 1\%$ ), and the other is based on all simulated cases which share the same minimum SEC with the first Pareto front.

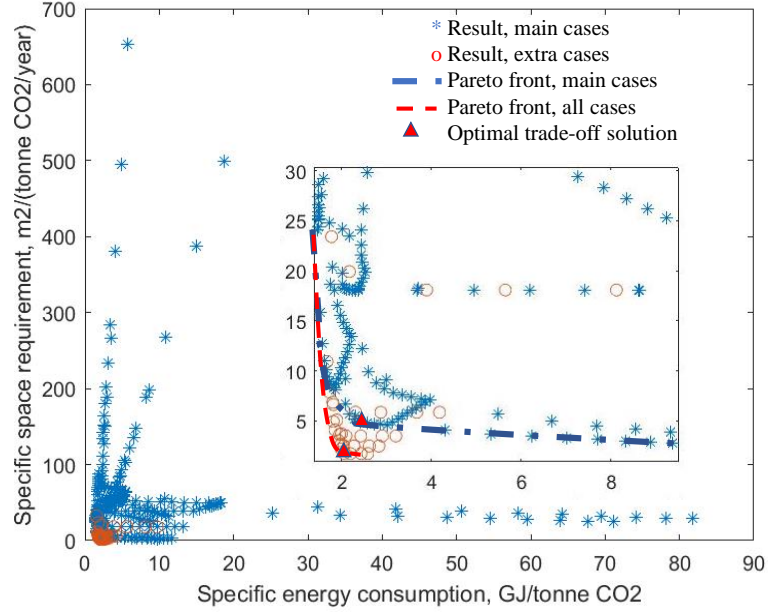


Fig. 7. Results of the main cases and the extra cases: specific space requirement (SSR) vs. specific energy consumption (SEC)

Table 3 shows the details of these cases and two additional designs representing the optimal trade-off between SEC and SSR along the two Pareto fronts, respectively, determined by visual inspection (marked in Fig. 7). The latter designs were predicted to achieve, respectively, a SEC of  $2.3 \text{ GJ tonne}^{-1}$  with a SSR at  $5.2 \text{ m}^2 (\text{tonne year}^{-1})^{-1}$  when  $x_{CO_2}^{inlet}$  is limited to 1%, and a slightly lower SEC of  $2.1 \text{ GJ tonne}^{-1}$  with a much lower SSR at  $1.8 \text{ m}^2 (\text{tonne year}^{-1})^{-1}$  when  $x_{CO_2}^{inlet}$  is allowed to rise to 10%.

Table 3. Attainable performance of the simulated cases

Parameter	Design with minimum energy consumption	Design with minimum space requirement		Design with optimal trade-off	
		From main cases	From all cases	From main cases	From all cases
Design ID	A	B	C	D	E
CO <sub>2</sub> feed fraction, $x_{CO_2}^{inlet}$	0.01	0.01	0.1	0.01	0.1
Packed bed height, $H_{bed}$ (m)	0.2	10.0	5.0	1.0	3.0
Particle diameter, $d_p$ (mm)	2.0	1.0	5.0	1.0	5.0
Superficial gas velocity, $u_G$ (m/s)	$1.0 \times 10^{-4}$	$1.0 \times 10^{-3}$	$1.0 \times 10^{-4}$	$5.0 \times 10^{-4}$	$1.0 \times 10^{-4}$
Superficial liquid velocity, $u_L$ (m/s)	$1.0 \times 10^{-4}$	$1.0 \times 10^{-4}$	$5.0 \times 10^{-5}$	$1.0 \times 10^{-4}$	$5.0 \times 10^{-5}$
<b>Total specific energy consumption (SEC, MJ/kg CO<sub>2</sub> captured)</b>	<b>1.467</b>	<b>9.798</b>	<b>2.196</b>	<b>2.285</b>	<b>2.054</b>
Energy consumption for particle preparation (MJ/kg CO <sub>2</sub> captured)	$1.035 \times 10^{-2}$	$5.170 \times 10^{-2}$	$2.584 \times 10^{-2}$	$4.835 \times 10^{-2}$	$2.701 \times 10^{-2}$
Energy consumption for pumping gas and liquid (MJ/kg CO <sub>2</sub> captured)	0.311	8.576	0.442	1.075	0.278
Energy consumption for CO <sub>2</sub> enrichment (MJ/kg CO <sub>2</sub> captured)	1.145	1.170	1.728	1.162	1.749
<b>Specific space requirement (SSR, m<sup>2</sup>/(tonne/year))</b>	<b>24.03</b>	<b>2.706</b>	<b>1.741</b>	<b>5.190</b>	<b>1.777</b>
Averaged CO <sub>2</sub> capture rate (kg/h per m <sup>2</sup> of reactor space)	$4.75 \times 10^{-3}$	$4.22 \times 10^{-2}$	$6.56 \times 10^{-2}$	$2.20 \times 10^{-2}$	$6.43 \times 10^{-2}$
Water consumption (m <sup>3</sup> /kg CO <sub>2</sub> captured)	72.830	8.483	2.745	16.306	2.799
Required time to dissolve 50 kg particle (h)	38,010	960	970	1980	950

Table 3 shows that only a small fraction of the total SEC (~1-2%) is required for supplying solid particles, across all the cases. The relative contributions of the other two SEC components, gas/liquid pumping and CO<sub>2</sub> enrichment, depend on (1) the performance indicator chosen for minimisation (compare e.g. designs A and B) – optimising for SEC as opposed to SSR would lead to a lower consumption by gas/liquid

pumping – and (2)  $x_{CO_2}^{inlet}$  (compare e.g. designs B and C) – operating at a higher  $x_{CO_2}^{inlet}$  would lead to a greater consumption by CO<sub>2</sub> enrichment, as expected. More detailed simulation results for the energy consumption breakdown can be found in [Section S3](#) of SI.

These results were derived from the numerical simulations which were conducted primarily for understanding the major impact of process parameters. These simulations did not provide an even coverage of the entire parametric space - better designs could probably be identified by rigorous optimisation. In any case, this is a simplified picture. For example, the specific space requirement took account of only the area of the weathering reactor and not the space required by the CO<sub>2</sub> enrichment system and other facilities; the energy demand calculation neglects factors such as pumping in seawater and pumping the liquid back to the sea which would consume additional energy.

### 3.2.3 Estimating losses due to the degassing of the liquid product

On the potential of CO<sub>2</sub> removal, the CCR calculated in the simulations took the weathering reactor as the system boundary. However, in an implemented scheme, the weathering product (the liquid effluent of the reactor) is expected to undergo degassing on transport into the ocean [\[9, 37\]](#) because the weathering reaction made use of enriched CO<sub>2</sub> concentrations (1%-10%) which are significantly above the atmospheric level. To estimate the loss of captured CO<sub>2</sub> due to degassing, additional modelling was carried out to predict the final composition of the reactor effluent when exposed to ambient air with a constant CO<sub>2</sub> concentration of 410 ppm ([Section S4](#) of SI). The results for designs D and E indicated respectively a rather significant 60% and 75% reduction in CCR to  $6.82 \times 10^{-3}$  and  $1.27 \times 10^{-2}$  kg/hour. These correspond to 0.55 (design D) and 0.62 (design E) moles of sustained CO<sub>2</sub> capture per mole of calcite dissolved, which is consistent with the previously suggested range of 0.4-0.7 moles of CO<sub>2</sub> capture by the dissolution of 1 mole of calcite in seawater [\[38\]](#). The loss of CO<sub>2</sub> caused by degassing would lead to a poorer performance of designs D and E with SEC increasing to 5.7 and 8.2 GJ tonne<sup>-1</sup> and SSR to 13.1 and 7.1 m<sup>2</sup> (tonne year<sup>-1</sup>)<sup>-1</sup>, respectively. Interestingly, design D (with 1% CO<sub>2</sub> feed) now appears to be more energy efficient than design E (with 10% CO<sub>2</sub> feed) after taking degassing into consideration, although the latter still retains a lower space

requirement. This result confirms the role of feed CO<sub>2</sub> concentration in balancing the trade-off between the two objectives.

In addition to degassing, the precipitation of carbonate from seawater and the release of additional CO<sub>2</sub> could further reduce the net CO<sub>2</sub> removal potential. Natural carbonate precipitation in seawater is thought to be primarily biologically controlled (see [38] and references therein), the analysis of which is beyond the scope of this work.

### **3.2.4 Comparison with other CDR options**

In an earlier study, we investigated calcite weathering with a counter-current trickle bed column (TBC) reactor, where a gas flows continuously upwards through a bed of mineral particles while liquid trickles down through in discrete rivulets [11]. This earlier work assumed the use of freshwater and focused on a CO<sub>2</sub> feed concentration at atmospheric level (i.e. 410 ppm); the effect of elevated CO<sub>2</sub> concentrations was considered only briefly. This earlier work only considered energy consumption for maintaining the liquid and gas flows and did not include the possible impact of degassing. Though direct comparison between the two studies is difficult, it can be seen that in terms of the specific energy consumption only for maintaining liquid and gas flows, the best simulated cases of the PBC reactor show a better performance than those reported for the TBC reactor. On the other hand, the TBC reactor was modelled with gas and liquid superficial velocities ( $u_G$  and  $u_L$ ) significantly greater than those for the PBC reactor, reflecting their different operability range. At the higher end of  $u_G$  ( $> 0.1 \text{ m s}^{-1}$ ) and  $u_L$  ( $> 1 \times 10^{-3} \text{ m s}^{-1}$ ) tested for the TBC reactor, which are outside the range considered for the PBC reactor, the TBC reactor was predicted with CCR values (before degassing) significantly greater than those of the PBC reactor in the present study. Industrial experience with packed bubble columns is much less than with TBCs, so experimental work is urgently required to explore the operating range of the PBC, and also to check the performance of both reactor systems with minerals of the type that might be used for enhanced weathering. This would underpin additional important future work in conducting rigorous optimisation of both reactor types with a comparable energy consumption accounting, to enable a reliable comparison, and perhaps the development of new reactor systems.

In the broader literature of CDR, the energy intensity of direct air capture (DAC) was recently suggested by McQueen et al. [39] to range from 2 – 10 GJ tCO<sub>2</sub><sup>-1</sup>. In another recent study [23], sorption processes using alkali scrubbing, MEA scrubbing and solid sorbent-based adsorption were assessed for DAC, suggesting energy consumption of 6.21-6.48, 20.04-49.32 and 7.96-8.68 MJ/kg CO<sub>2</sub>, respectively, with the two ends of the range for each option representing extreme positions in the “energy consumption vs. productivity” trade-off. It is worth to mention that research on DAC has identified some of its major challenges with respect to energy consumption, among which is the need for overcoming pressure drop in a system involving a gas-liquid contractor processing a highly diluted gas flow [40], an issue that has also been shown to be important in the enhanced weathering reactor investigated in this work particularly with higher gas flow rates. Besides DAC studies, energy usage for EW of rocks typically ranges 0.1-8.4 GJ tCO<sub>2</sub><sup>-1</sup> [38], while 1.5 GJ tCO<sub>2</sub><sup>-1</sup> was reported in a study based on direct mineralisation [41]. For comparison with seawater-based methods, ocean liming generally takes 6-10 GJ tCO<sub>2</sub><sup>-1</sup> [34, 38], while electrochemical weathering in seawater may have an associated energy usage of 6-8 GJ tCO<sub>2</sub><sup>-1</sup> [37, 42]. The various levels of technological development, testing and implementation of these other CCS technologies, as well as energy incursions associated with regional distinctions (e.g., ocean liming in coastal regions), means direct comparison has inherent uncertainties. Nevertheless, the predicted energy efficiency of the reactor scheme modelled in this work, after the estimated deduction by degassing, is within the range of the other CDR options.

#### 4. Conclusions

A process is presented for removing carbon dioxide from the atmosphere and dissolving it in seawater. Using a mathematical model with its key mass transfer and chemical reaction components validated with experimental data, this work specifies an engineered system based on a packed bubble column reactor with CO<sub>2</sub> enrichment of the air stream. This system captures atmospheric CO<sub>2</sub> into dissolved inorganic carbon that can readily be stored in the sea, with potential to offer a CDR implementation at an energy consumption level within the broad range of other CDR options. The assessment was based on the use of seawater as opposed to freshwater, to overcome the barrier of high water usage in such engineered schemes. The spatial

requirement was also estimated which, although currently limited to the ground area occupation of the weathering reactor, offers a starting point for further assessing operational feasibility. This work calculated the likely impact of operational settings such as gas and liquid velocities, particle size, bed height and feed CO<sub>2</sub> concentration, and revealed the dominance of pumping liquid and gas flows in total energy consumption and the significant trade-off between energy consumption and space requirement. These investigations highlight the importance of detailed engineering design and analysis in developing future CDR technologies.

Two particular areas for further research are highlighted. First, the specific reactor type considered in this study, the packed bubble column reactor, is much less well researched than other gas-liquid-solid reactors, particularly with regard to the mass transfer-related characteristics of crushed rock. Second, the assessed CDR scheme is essentially a hybrid system that combines CO<sub>2</sub> enrichment (a variant of DAC) with mineral weathering. There is need for research - innovation, experiment and modelling - tailoring DAC schemes for use in such hybrids, making use of their potential to produce economically an air feed stream enriched in CO<sub>2</sub>.

### **Acknowledgement**

The authors acknowledge the financial support by the Greenhouse Gas Removal by Enhanced Weathering (GGREW) project (grant No. NE/P01982X/1) funded by the Natural Environment Research Council (NERC) of the UK.

### **References**

1. IPCC. Summary for policymakers. In: Masson-Delmotte V, Zhai P, Pörtner HO, et al., eds. Global Warming of 1.5 °C. An IPCC Special Report on the Impacts of Global Warming of 1.5 °C Above Pre-Industrial Levels and Related Global Greenhouse Gas Emission Pathways, in the Context of Strengthening the Global Response to the Threat of Climate Change, Sustainable Development, and Efforts to Eradicate Poverty. Geneva, Switzerland: World Meteorological Organization; 2018:32.
2. Greenhouse Gas Removal. The Royal Academy of Engineering, 2018.
3. National Academy of Sciences Engineering and Medicine. Negative Emissions Technologies and

Reliable Sequestration. Washington, DC: National Academies Press, 2019.

4. Hartmann J, West AJ, Renforth P, et al. Enhanced chemical weathering as a geoengineering strategy to reduce atmospheric carbon dioxide, supply nutrients, and mitigate ocean acidification. *Rev. Geophys.* 2013; 51: 113-149.
5. Hartmann J, Jansen N, Dürr HH, et al. Global CO<sub>2</sub>-consumption by chemical weathering: What is the contribution of highly active weathering regions? *Glob. Planet Change.* 2009; 69: 185-194.
6. Renforth P, Pogge von Strandmann PAE, Henderson GM. The dissolution of olivine added to soil: Implications for enhanced weathering. *Appl. Geochem.* 2015; 61: 109-118.
7. Beerling DJ, Kantzas EP, Lomas MR, et al. Potential for large-scale CO<sub>2</sub> removal via enhanced rock weathering with croplands. *Nature.* 2020; 583: 242-248.
8. Montserrat F, Renforth P, Hartmann J, et al. Olivine Dissolution in Seawater: Implications for CO<sub>2</sub> Sequestration through Enhanced Weathering in Coastal Environments. *Environ. Sci. Technol.* 2017; 51: 3960-3972.
9. Rau GH. CO<sub>2</sub> Mitigation via Capture and Chemical Conversion in Seawater. *Environ. Sci. Technol.* 2011; 45: 1088-1092.
10. Hamilton JL, Wilson SA, Morgan B, et al. Accelerating Mineral Carbonation in Ultramafic Mine Tailings via Direct CO<sub>2</sub> Reaction and Heap Leaching with Potential for Base Metal Enrichment and Recovery. *Econ Geol.* 2020; 115: 303-323.
11. Xing L, Darton RC, Yang AD. Enhanced weathering to capture atmospheric carbon dioxide: Modeling of a trickle-bed reactor. *AIChE J.* 2021; 67: e172020.
12. Cooke RC, Kepkay PE. Apparent calcite supersaturation at the ocean surface: Why the present solubility product of pure calcite in seawater does not predict the correct solubility of the salt in nature. *Mar. Chem.* 1984; 15: 59-69.
13. Danckwerts PV. Continuous flow systems: distribution of residence times. *Chem. Eng. Sci.* 1995; 50: 3857-3866.
14. Cents AHG, Brilman DWF, Versteeg GF. CO<sub>2</sub> absorption in carbonate/bicarbonate solutions: The

- Danckwerts-criterion revisited. *Chem. Eng. Sci.* 2005; 60: 5830-5835.
15. Plummer LN, Busenberg E. The solubilities of calcite, aragonite and vaterite in CO<sub>2</sub>-H<sub>2</sub>O solutions between 0 and 90°C, and an evaluation of the aqueous model for the system CaCO<sub>3</sub>-CO<sub>2</sub>-H<sub>2</sub>O. *Geochim. Cosmochim. Acta.* 1982; 46: 1011-1040.
  16. Naviaux JD, Subhas AV, Rollins NE, et al. Temperature dependence of calcite dissolution kinetics in seawater. *Geochim. Cosmochim. Acta.* 2019; 246: 363-384.
  17. Akita K, Yoshida F. Gas holdup and volumetric mass transfer coefficient in bubble columns: effect of liquid properties. *Ind. Eng. Chem. Res.* 1973; 12: 76-80.
  18. Maldonado JGG, Bastoul D, Baig S, et al. Effect of solid characteristics on hydrodynamic and mass transfer in a fixed bed reactor operating in co-current gas-liquid up flow. *Chem. Eng. Process.* 2008; 47: 1190-1200.
  19. Taghavi M, Balakotaiah V. Gas hold-up and bubble behavior in an upflow packed bed column in the limit of low flow rate. *AIChE J.* 2019; 65: 16624.
  20. Darton RC. Physical behaviour of three-phase fluidized beds. *Fluidization.* 1985; 495-528.
  21. Collins JHP, Sederman AJ, Gladden LF, et al. Characterising gas behaviour during gas-liquid co-current up-flow in packed beds using magnetic resonance imaging. *Chem. Eng. Sci.* 2017; 157: 2-14.
  22. Danckwerts PV. Significance of Liquid-Film Coefficients in Gas Absorption. *Ind. Eng. Chem. Res.* 1981; 43:1460-1467.
  23. Sabatino F, Grimm A, Gallucci F, Van Sint Annaland, M, Kramer GJ, Gazzani M. A comparative energy and costs assessment and optimization for direct air capture technologies. *Joule.* 2021; 5: 2047-2076.
  24. Darton RC, Yang A. Removing carbon dioxide from the air to stabilise the climate, in *Advances in Carbon Management Technologies*, eds. S. K. Sidkar and F. Priciotta (Boca Raton: CRC Press), 2020, 3-22.
  25. Wilcox J, Psarras PC, Liguori S. Assessment of reasonable opportunities for direct air capture. *Environ. Res. Lett.* 2017; 12: 065001.



26. Elfving J, Kauppinen J, Jegoroff M, Ruuskanen V, Jarvinen L, Sainio T. Experimental comparison of regeneration methods for CO<sub>2</sub> concentration from air using amine-based adsorbent. *Chem. Eng. J.* 2021; 404: 126337.
27. Shigenori F, Selyanchyn R, Kunitake T. A new strategy for membrane-based direct air capture, *Polymer J.* 2021; 53:111-119.
28. Mahdi F, Olga E, Christian B. Techno-economic assessment of CO<sub>2</sub> direct air capture plants. *J. Clean. Prod.* 2019; 224: 957-980.
29. White SD, Yarrall MG, Cleland DJ, et al. Modelling the performance of a transcritical CO<sub>2</sub> heat pump for high temperature heating. *Int. J. Refrig.* 2002; 25: 479-486.
30. Sun S, Guo H, Lu D, et al. Performance of a single-stage recuperative high-temperature air source heat pump. *Appl. Therm. Eng.* 2021; 193: 116969.
31. CIPEC. Benchmarking the energy consumption of Canadian open-pit mines. Mining Association of Canada and Natural Resources Canada, 2005.
32. Norgate T, Haque N. Energy and greenhouse gas impacts of mining and mineral processing operations. *J. Clean. Prod.* 2010; 18: 266-274.
33. Traverso M, Rizzo G, Finkbeiner M. Environmental performance of building materials: life cycle assessment of a typical Sicilian marble. *Int. J. Life Cycle Assess.* 2010; 15: 104-114.
34. Renforth P, Jenkins BG, Kruger T. Engineering challenges of ocean liming. *Energy.* 2013; 60: 442-452.
35. Julia S, Kirchner KA, Lettmann BS, et al. Carbon capture via accelerated weathering of limestone: Modeling local impacts on the carbonate chemistry of the southern North Sea. *Int. J. Greenh. Gas Control.* 2020; 92: 102855.
36. Harvey L. Mitigating the atmospheric CO<sub>2</sub> increase and ocean acidification by adding limestone powder to upwelling regions. *J. Geophys. Res.* 2008; 113: C04028.
37. Rau GH. Electrochemical splitting of calcium carbonate to increase solution alkalinity: implications for mitigation of carbon dioxide and ocean acidity. *Enviro. Sci. Technol.* 2008; 42: 8935-8940.

38. Renforth P, Henderson G. Assessing ocean alkalinity for carbon sequestration. *Rev. Geophys.* 2017; 55: 636-647.
39. McQueen N, Gomes KV, McCormick C, Blumanthal K, Pisciotta M, Wilcox J. A review of direct air capture (DAC): scaling up commercial technologies and innovating for the future. *Prog. Energy* 2021; 3: 032001.
40. American Physical Society, Direct Air Capture of CO<sub>2</sub> with Chemicals, 2011.
41. Myers C, Nakagaki T. Direct mineralization of atmospheric CO<sub>2</sub> using natural rocks in Japan. *Environ. Res. Lett.* 2020; 15: 124018.
42. Rau GH, Carroll SA, Bourcier WL, et al. Direct electrolytic dissolution of silicate minerals for air CO<sub>2</sub> mitigation and carbon-negative H<sub>2</sub> production. *Proc. Natl. Acad. Sci.* 2013; 110: 10095-10100.
43. Dickson AG, Millero FJ. A comparison of the equilibrium constants for the dissociation of carbonic acid in seawater media: Dickson, A.G. and F.J. Millero, 1987. *Deep-Sea Res.*, 34:1733-1743.
44. Millero FJ. Thermodynamics of the carbon dioxide system in the oceans. *Geochim. Cosmochim. Acta.* 1995; 59: 661-677.
45. Johnson KS. Carbon dioxide hydration and dehydration kinetics in seawater. *Limnol. Oceanogr.* 1982; 27: 849-855.
46. Plummer LN, Wigley TML, Parkhurst DL. The kinetics of calcite dissolution in CO<sub>2</sub>-water system at 5° to 60 °C and 0.0 to 1.0 atm CO<sub>2</sub>. *Amer. J. Sci.* 1978; 278: 179-216.